

ENSEMBLES OF CLIMATE CHANGE MODELS FOR RISK ASSESSMENT OF NUCLEAR POWER PLANTS

Matteo Vagnoli¹, Francesco Di Maio^{2*}, Enrico Zio^{2,3}

¹*Resilience Engineering Research Group*

Faculty of Engineering, University of Nottingham

University Park Nottingham, NG7 2RD

²*Energy Department, Politecnico di Milano*

Via La Masa 34, 20156 Milano, Italy

*Corresponding author: francesco.dimaio@polimi.it

³*Chair on System Science and Energetic Challenge*

Fondation Electricite de France (EDF), CentraleSupélec,

Univerisite Paris Saclay, Voie des Vignes 92290, Chatenay-Malabry, France

ABSTRACT

Climate change affects technical Systems, Structures and Infrastructures (SSIs), changing the environmental context for which SSI were originally designed. In order to prevent any risk growth beyond acceptable levels, the climate change effects must be accounted for into risk assessment models. Climate models can provide future climate data, such as air temperature and pressure. However, the reliability of climate models is a major concern due to the uncertainty in the temperature and pressure future projections. In this work, we consider five climate change models (individually unable to accurately provide historical recorded temperatures and, thus, also future projections), and ensemble their projections for integration in a probabilistic safety assessment, conditional on climate projections. As case study, we consider the Passive Containment Cooling System (PCCS) of two AP1000 Nuclear Power Plants (NPPs). Results provided by the different ensembles are compared. Finally, a risk-based classification approach is performed to identify critical future temperatures, which may lead to PCCS risks beyond acceptable levels.

Keywords: Probabilistic safety assessment; Climate change; Ensemble of climate models; Risk-based classification; Passive Containment Cooling System (PCCS); Nuclear Power Plant (NPP).

1. INTRODUCTION

The Intergovernmental Panel on Climate Change (IPCC) has underlined the need of placing increasing emphasis on the assessment of the impact of global climate change on the reliability of critical Systems, Structures and Infrastructures (SSIs) [1]. Climate change must be embedded into risk assessment to take into account the changing environmental context, and avoid or mitigate unexpected and undesirable operational conditions that were not considered in the SSIs design phase. Current climate change seems to go beyond the bounds of the natural cyclic changes and how the natural, social and technical systems can tolerate this is a major issue [2]. To mention one phenomenon that might affect the cooling capability of risk-relevant SSIs, (like Nuclear Power Plants (NPPs)), a global average surface temperature increase of about 0.8°C has been recorded since 1900, and is expected to reach even 6.4°C by 2100 (depending on future Green House Gas (GHG) emissions and human activity [3; 4; 5; 6]), endangering cooling capability of SSIs.

The large uncertainties on the impact of climate change on the operational risk of SSIs rises significant challenges and methods are needed that allow assessing the possible impact of climate change with a transparent and feasible treatment of the involved uncertainties [1]

Risk assessment methods typically rely on probabilistic-based approaches, wherein uncertainties are propagated into the risk model output [7]. In this framework, the uncertainty in the climate change projections, i.e. the uncertainty of the future values given by a climate model [8], plays an important role because it may lead either to over- or to under-estimation of the risk. In this respect, a pool of climate change models is available, each one addressing a specific problem (for example, the cause-effect relationship between climate change and GHG emissions), but none can be identified as the single best climate model [3]. The problem is, then, one of model uncertainty [9]. The difficulty in quantifying and managing this source of uncertainty is a challenge. Bayesian approaches have been proposed [9; 10; 11; 12; 13], but in the climate change modelling problem, the lack of comprehensive climate models, which treat all the specific issues addressed by the individual models, calls for aggregating the different models into an ensemble [14]. In this paper, three ensemble approaches are investigated to aggregate the projections of five climate models to improve the robustness and the accuracy of the projection of the future climate conditions [15; 16; 17; 18; 19; 20]. We aggregate the climate projections of five models (under one climate pathway of global future development (RCP 6.0)) from the open-source database Climate Change Health Impact Profiles project (ClimateCHIP, www.climatechip.org). The ensemble approaches of aggregation differ in the way they score the different models with respect to the monthly Mean Absolute Error (MAE), which is computed (for each climate model) by assessing the difference between the recorded and computed air temperature

recorded (from 1981 to 2005). The following weighting strategies are considered for the aggregation [15; 16; 21]: *i*) weight proportional to the inverse of the MAE; *ii*) weight proportional to the logarithm of the inverse of the MAE; *iii*) weight proportional to a Borda count-based ranking [15]. We consider the Passive Containment Cooling System (PCCs) of AP1000 NPPs as case study [22] because: *i*) nuclear power is an energy option considered to reduce greenhouse gas emissions [23; 24]; *ii*) it has been shown that the safety and reliability of NPPs are significantly influenced by changes of air temperature, precipitation, river flows, sea level, shoreline erosion, coastal storms, floods, heat waves, etc., that affect cooling water supply [2; 8; 25; 26; 27].

The proposed ensemble methods are used to aggregate the forecasts of the climate change models in order to assess the Conditional Functional Failure Probability (CFFP) of the PCC by performing for, an integrated probabilistic safety assessment conditional on climate projections [22; 28] and to classify the temperature conditions that lead the PCCS to unexpected and dangerous scenarios [28]. The CFFP is the probability that the pressure of the containment exceeds a safety threshold, and it is computed by carrying out a Monte Carlo (MC) sampling of all input variables of the thermo-hydraulic model, which simulates the PCCS after a Loss Of Coolant Accident (LOCA). The results provided with the ensemble of temperature projections are compared with those retrieved using the individual climate change models. On the other hand, the great benefit of the risk-based classification approach consists in that once the air temperature projections of the different climate models (ensemble or not) are compared to the risk-relevant temperature interval, the risk assessment and the climate projections are simultaneously provided.

The remaining of this paper is organized as follows: Section 2 introduces the characteristics of the PCCS, and its behaviour following a LOCA; the climate models and their ensemble alternative strategies are described in Section 3; the theoretical description of the proposed risk assessment analyses is provided in Section 4; results of the risk assessment are presented in Section 5; conclusion and remarks are discussed in Section 6.

2. THE CASE STUDY

In this work, the Passive Containment Cooling System (PCCS) of the Westinghouse AP1000 Pressurized Water Reactor (PWR) is considered (Fig. 1) [29]. The AP1000 has been the first Generation III+ reactor to receive the final design certification by the Nuclear Regulatory Commission of the United States (U.S. NRC) in 2005, and has been built (or is planned to be built) worldwide. The relevance of the considered system becomes clear by looking at Fig. 2, where the locations of the 15 plants that are (at present time) operating in the world or planned to be constructed are shown [www.world-nuclear.org].

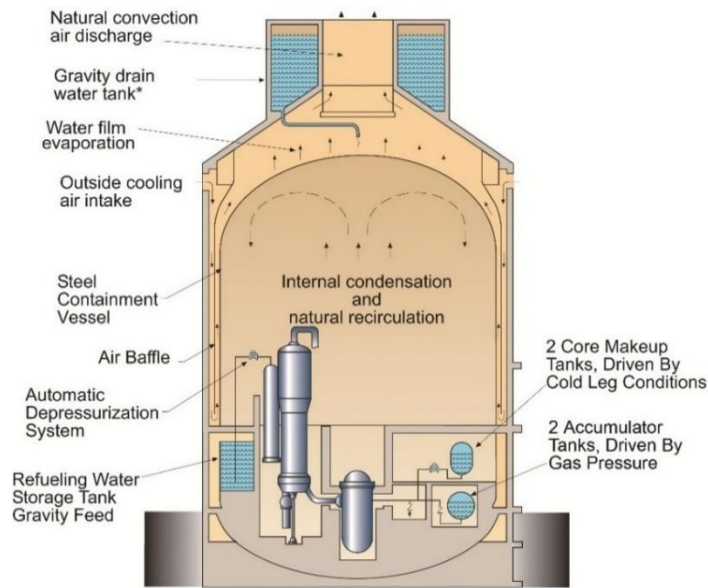


Fig. 1 An AP1000 Passive Containment Cooling System.

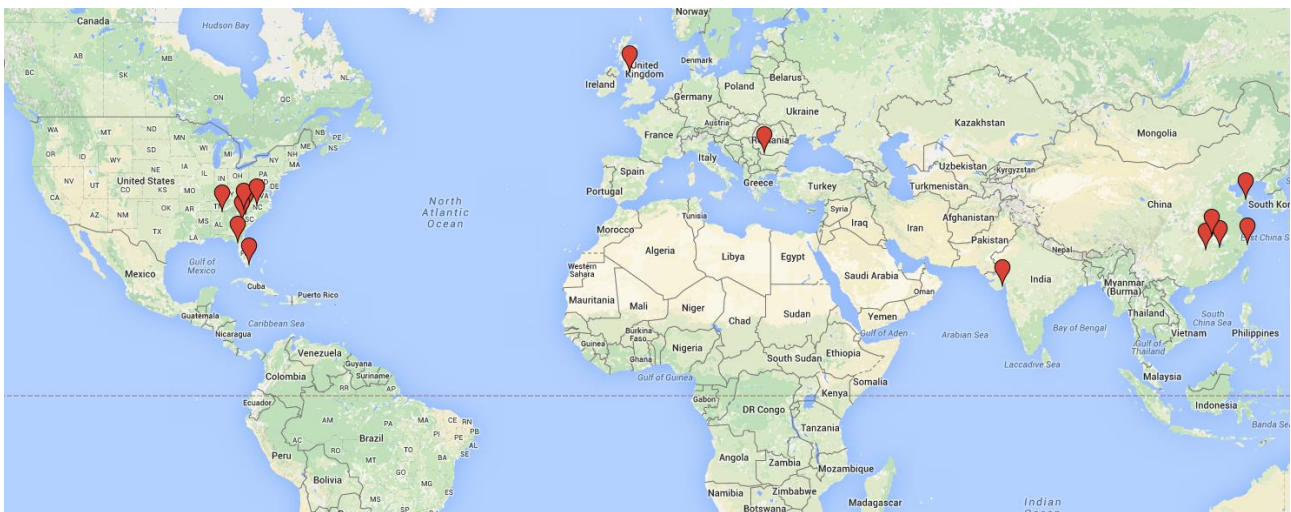


Fig. 2 The locations of the operating and planned AP1000.

Following an accident, the PCCS cools the containment vessel in a passive way, which means that its operation is not triggered by electricity. The natural circulation of the air within the containment shield building enhanced by the evaporation of the water, which is drained by gravity from a pool situated on top of the containment shield building, removes heat from the containment vessel. If the pressure is effectively controlled within the safety limit of 0.4 MPa after 1000 seconds from the beginning of the accidental scenario, the removal of heat is successful and safety guaranteed [30]. The accident considered is a Loss of Coolant Accident (LOCA) [31] and it is modelled resorting to a Thermal Hydraulic (TH) model of literature [22; 29].

The evolution of a LOCA is typically described by four steps [32]: (1) blowdown, from the accident beginning to the time at which the primary circuit pressure is equal to the containment pressure; (2) refill, from the end of the blowdown to the time when the vessel lower plenum is completely refilled by the Emergency Core Cooling System (ECCS); (3) reflood, which is the interval of time in which the core is flooded by water; (4) post-reflood, which starts after the core is completely quenched and ends when the energy is released to the Reactor Coolant System (RCS). In the post-reflood phase, the steam produced in the RCS is cooled at the internal layer of the steel containment vessel and, then, the heat is conducted by the vessel and transferred to the atmosphere in the air channels. The outside cooling cold air enters the channels through the three rows of air inlets and flows down to the bottom of the channels, where it is heated by the steel vessel up to the air diffuser to the environment, as shown in Fig. 1.

The Functional Failure Probability (FFP) of the PCCS of the AP1000 due to a LOCA, which is the probability of the containment pressure to exceed the safety limit of 0.4 MPa, is then quantified by using the TH model. The TH model uses 24 input variables, such as the diffusive coefficient (D_{cf}) or the diameter of the air outlet tube (D_{ot}). The design input variables are listed in Table 1, together with their distributions chosen from expert judgment and literature review [7; 33; 34]. The last two variables, which describe the surrounding environmental conditions and have to be used as input of the TH model, are the air temperature T , and the air pressure A . The output variable is the pressure value of the containment pressure Y , after 1000 s from the beginning of the LOCA.

Table 1 List of parameters distributions.

<i>Parameter</i>	<i>Unit</i>	<i>Type of distribution</i>	<i>Mean value μ</i>	<i>Standard deviation σ</i>
LOCA steam temperature	°C	normal	250	5
LOCA steam pressure	MPa	normal	0.1	5
Water density in primary circuit	kg/m ³	normal	666.7	2
Pressure of primary circuit	MPa	normal	15.5	2
Containment volume	m ³	normal	58333	1
Containment wall thickness	m	Normal	0.04455	0.5
Containment diameter	m	Normal	39.62	0.5
Containment height	m	Normal	34.12	0.5
Width of air baffle outside containment	m	Normal	0.92	0.5
Height of the download in air baffle	m	Normal	38.11	0.5
Height of the upload in air baffle	m	Normal	59.89	0.5
Diameter of the air outlet	m	Normal	9.75	0.5
Height of the air outlet	m	Normal	6	0.5
Diameter of uphead	m	Normal	39.62	0.5
Height of	m	Normal	11.47	0.5

uphead				
Diffusive coefficient (water)	m ² /s	Normal	2.55E-05	20
Heat conduction of the wall	W/mK	Normal	54	5
<i>Description</i>	<i>Unit</i>	<i>Type of Distribution</i>	<i>Lower value</i>	<i>Upper value</i>
Air channel rugosity	-	Uniform	0.00285	0.00315
Friction factor of corner	-	Uniform	0.475	0.525
Friction factor of inlet	-	Uniform	0.9025	0.9975
Friction factor of pipeup	-	Uniform	0.1425	0.1575
Friction factor of pipeout	-	Uniform	0.1425	0.1575
Friction factor of pipecold	-	Uniform	0.1425	0.1575
Steady state LOCA mass flow rate	kg/s	Uniform	6	11

3. Ensembles of climate projection data

The AP1000 NPPs are design to operate for 80 to 100 years. It is, then, reasonable to investigate how the climate change and, in particular, the change of air temperature and pressure, might affect the reliability performance and the risk of these NPPs.

To this aim, the air temperature forecast $T^{projected}$ from the ClimateCHIP site (www.climatechip.org) has been taken. Five different climate models, developed within the Coupled Model Intercomparison Project (CMIP5) (the most relevant global project aimed at analysing the past and predict the future climate changes [35]), have been considered:

1. the USA GFDL-esm2m (GFDL) model [36];
2. the UK HadG-EM2-es (HadGem) model [14];
3. the French IPSL-CM5a-lr (IPCM) model [37];
4. the Japanese MIROC-esm-chem (MIROC) model [38];
5. the Norwegian NORESM1-m (NORES) model [39].

Each model provides the monthly mean $T_{mean}^{projected}$ and the maximum $T_{max}^{projected}$ air temperatures for four intervals of years (from 1981 to 2099): t_1 from 1981 to 2005, t_2 from 2011 to 2040, t_3 from 2041 to 2070 and t_4 from 2071 to 2099. The Representative Concentration Pathway (RCP) 6.0 assumption, which considers an equilibrium scenario of the total radiative force after the year 2100, due to a reduction of the GHG emission, has been adopted to retrieve the climate data [40].

A weighting strategy is utilized for aggregating future air temperatures [42], which are provided in terms of statistical indicators like the mean value (if the forecasts of the air temperatures were provided in the form of probability distributions, these could be aggregated by Bayesian model averaging [41]). The weighting is based on the difference between the predicted air temperature values and the real air temperature data in the time interval t_1 , from 1981 to 2005. For each AP1000 location of Fig 2, the values of the air temperature provided by each climate model in the t_1 time interval can be compared with the real air temperatures recorded in the same location, during the same period of time. The historical recorded temperatures have been retrieved by two historical databases provided by the National Oceanic and Atmospheric Administration (NOAA) [<https://www.ncdc.noaa.gov>] and by the National Aeronautics and Space Administration (NASA) [43; 44].

At each month i , a weight w_j , is associated to each j -th climate model. The weight w_j of the j -th climate change model is calculated for each month i as to the Mean Absolute Error (MAE) of the j -th climate model projection $T_i^{\text{projected}}$ (where $T_i^{\text{projected}}$ is either $T_{\text{mean}}^{\text{projected}}$ or $T_{\text{max}}^{\text{projected}}$ of the j -th climate model):

$$MAE_{ji} = \frac{\text{abs}(T_i^{\text{real}} - T_i^{\text{projected}})}{12} \quad \forall i = 1, 2, \dots, 12; j = 1, 2, \dots, 5 \quad (1)$$

For example, let us consider the NPP in Samen County, Zhejiang Province, China (as shown by a pin in Fig. 3). The historical air temperatures are retrieved from the NOAA and NASA databases, which provide the temperatures of three weather stations nearby the NPP (shown with stars in Fig. 3). The historical values T_i^{real} , $i=1,2,\dots,12$, are assumed as the mean air temperatures recorded by the three weather stations for each i -th month in the time interval from 1981 to 2005. It is worth underling that since air temperature is strongly correlated for weather stations that are separated by up to 1200 km [45], in this case, although the weather stations are not placed closely to the NPP, the T_i^{real} approximation is reasonable.

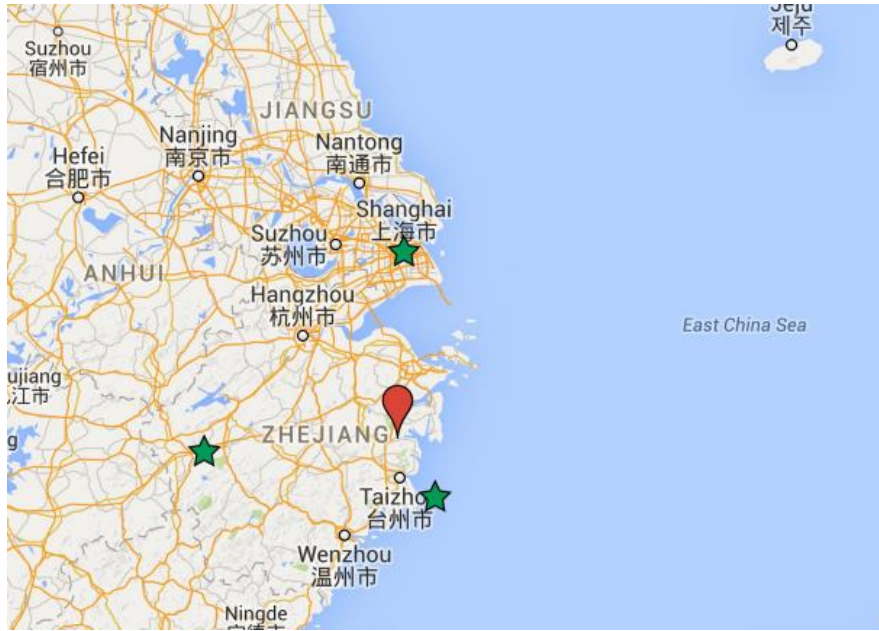


Fig. 3 The Sanmen NPP (pin) and the correlated three weather stations (stars).

Fig. 4 shows the difference between the T_i^{real} (solid line) and the $T_i^{projected}$ (taken equal to $T_{mean}^{projected}$) values for each j -th climate model. It is worth noting that from April (month 4) to August (month 8) all the climate models underestimate T_i^{real} .

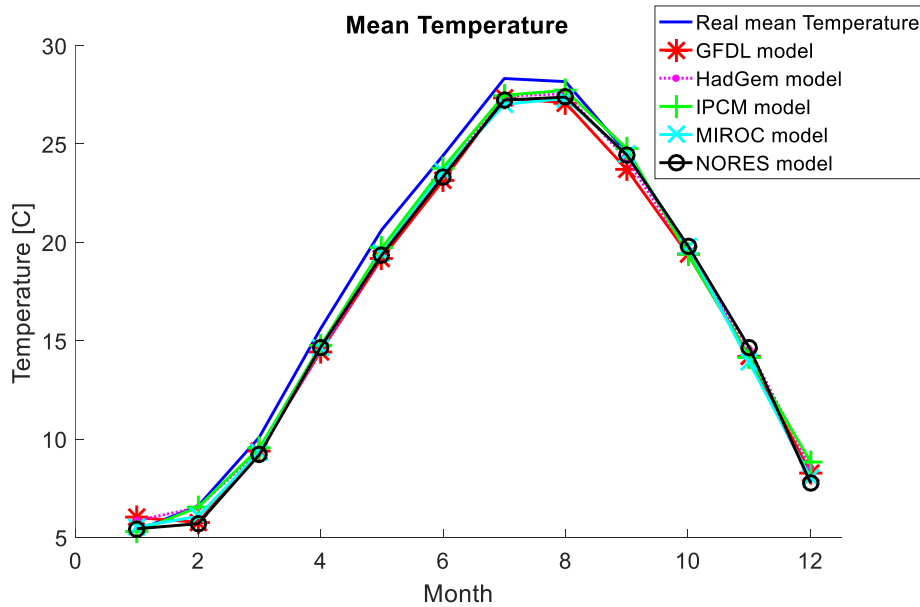


Fig. 4 The real recorded air temperatures (solid line) and those provided by the climate models in the time interval from 1981 to 2005.

Fig. 5 shows a more accurate representation of the difference along the period t_1 between T_i^{real} and $T_i^{projected}$ (again taken equal to $T_{mean}^{projected}$) for each model. Each bar corresponds to one month of the year. Again, the largest discrepancy is reached in the period April-August (i.e. the fourth, fifth, sixth, seventh and eighth bars of each model are the highest). The climate change models perform small errors during the cold months (i.e. January, February, October, November and December, that are the first, second and last three bars of each model, respectively, in Fig. 5). Also, as all climate change model commit errors, it is not easy to identify the best one. For example, even if the IPCM model seems to overcome the other models (almost) throughout the 12 months, in December it shows the largest error over all models.

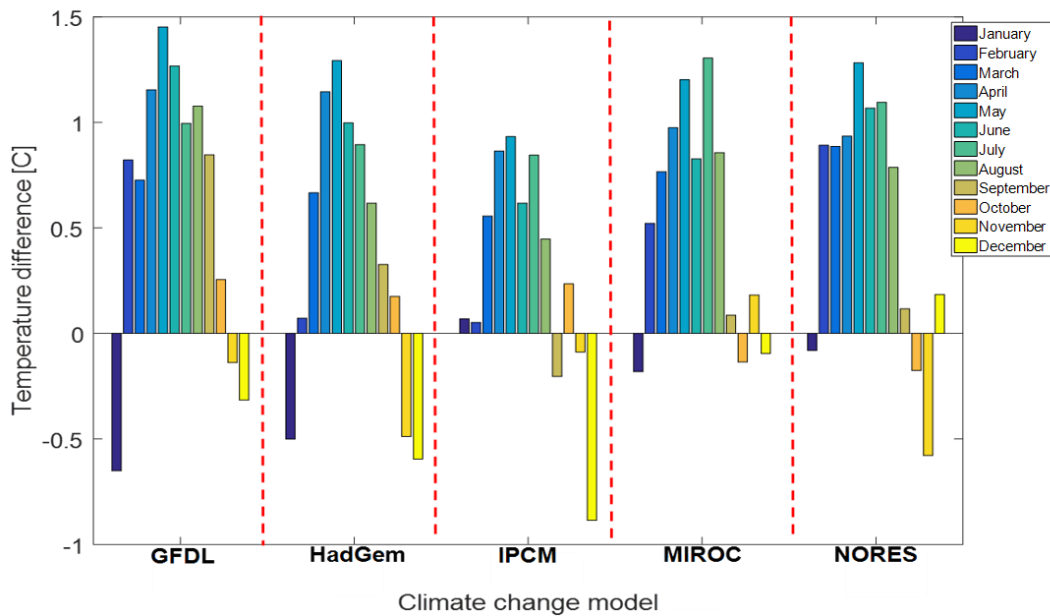


Fig. 5 Difference between the temperatures provided by each individual climate change model and the real air temperatures for each month in the time interval from 1981 to 2005.

To improve projection accuracy, a procedure of aggregation of the climate change models into an ensemble is introduced. Three ensemble approaches, which differ on the definition of the considered weighting strategies, are defined in order to obtain a projection that relies on the strengths of each single climate method. Hence, each climate model is rewarded with a weight that is influenced by the accuracy of the considered model, and consequently the most accurate model is awarded with the highest weight. It should be noted that the weights do not necessarily sum to 1, but rather the larger the weight is assigned to each model, the better its performance in approximating the real air

temperature in the time interval from 1981 to 2005. The three ensemble approaches can be defined as follows [19]:

- a) weight proportional to the inverse of the MAE [42]:

$$w_{ij} = \frac{1}{MAE_{ij}} \quad \forall i = 1, 2, \dots, 12; j = 1, 2, \dots, 5 \quad (2)$$

- b) weight proportional to the logarithm of the inverse of the MAE [42]:

$$w_{ij} = \log \left(\frac{\max(MAE_{ij})}{MAE_{ij}} \right) \quad \forall i = 1, 2, \dots, 12; j = 1, 2, \dots, 5 \quad (3)$$

where $\max(MAE_{ij})$ is the maximum error between the temperatures predicted by the climate change models and the real air temperature values, for each month.

- c) For each month, a weight proportional to a Borda count-based ranking [15] is assigned to each model. The ranking score $S \in [1, 50]$ is equal to 1 for the (worst) model with the largest MAE, and 50 for the best performing climate change model with the smallest MAE. Consequently, the higher the rank, the higher the weight assigned to the climate model, allowing the best performing climate model to bring more information in the ensemble (more than for strategy *b*).

Once the weight, w_{ij} , is defined, the air temperatures predicted by each climate change model are aggregated into the predicted temperature T_i , by computing the simple average:

$$T_i = \sum_{j=1}^5 \frac{T_j^{\text{projected}} \cdot w_j}{MAE_{tot}} \quad \forall i = 1, 2, \dots, 12 \quad (3)$$

where MAE_{tot} is the sum of the MAE_j of each individual climate change model. Again, Eq. (3) shows that the aggregated air temperature T_i is expected to provide a more accurate temperature projection

than the individual models projections, because the better the accuracy of the individual climate model is, the smaller its MAE and the larger its weight in the ensemble.

Fig. 6 shows the differences between T_i^{real} and the ensembled air temperatures T_i using the three abovementioned strategies *a*), *b*), *c*) (where each bar corresponds to the *i*-th month). Although the ensemble strategies commit errors in the warmest months of the year (from April to September), these are smaller than those committed by the individual climate models of Fig. 5. Especially, the Borda count-based ranking (strategy *c*) shows the largest accuracy because the error committed in the temperature estimation during the cold months (from October to February) is almost negligible.

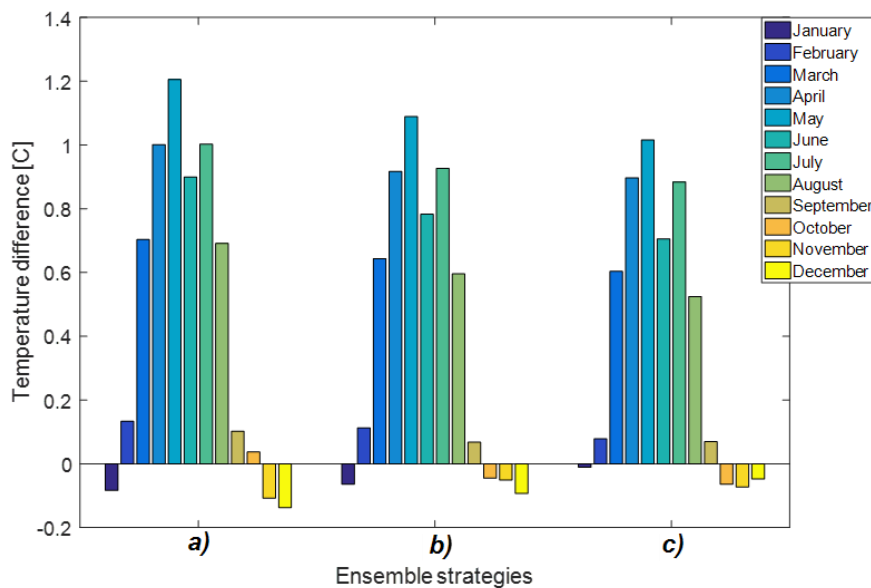


Fig. 6 Difference between ensembled temperatures with strategies *a*), *b*) and *c*) and the real air temperature, in the time interval from 1981 to 2005.

The performances of the ensemble strategies and of the individual models have been exhaustively calculated for all the 15 AP1000 power plants of Fig 2, and reported in Fig. 7. For each NPP, the real air temperature data have been retrieved from the repository of the NASA and NOAA database for the closest weather station to the plant. Fig. 7 summarizes the results, for each NPP site of Fig 2: the mean error committed along the 12 months considered is compared among the individual climate models and the ensemble strategies. It is worth highlighting that the ensemble strategies of the climate change models show better accuracy than the individual climate change models in all 15 NPP sites around the world, i.e., the error between the real air temperature and those obtained by applying the ensemble of the climate change models is lower than for the individual climate models. In particular,

the results for site 11 (i.e., the Duke's Lee NPP, in Gaffney, South Carolina, USA) shows that the ensemble strategies reduce to almost zero the error.

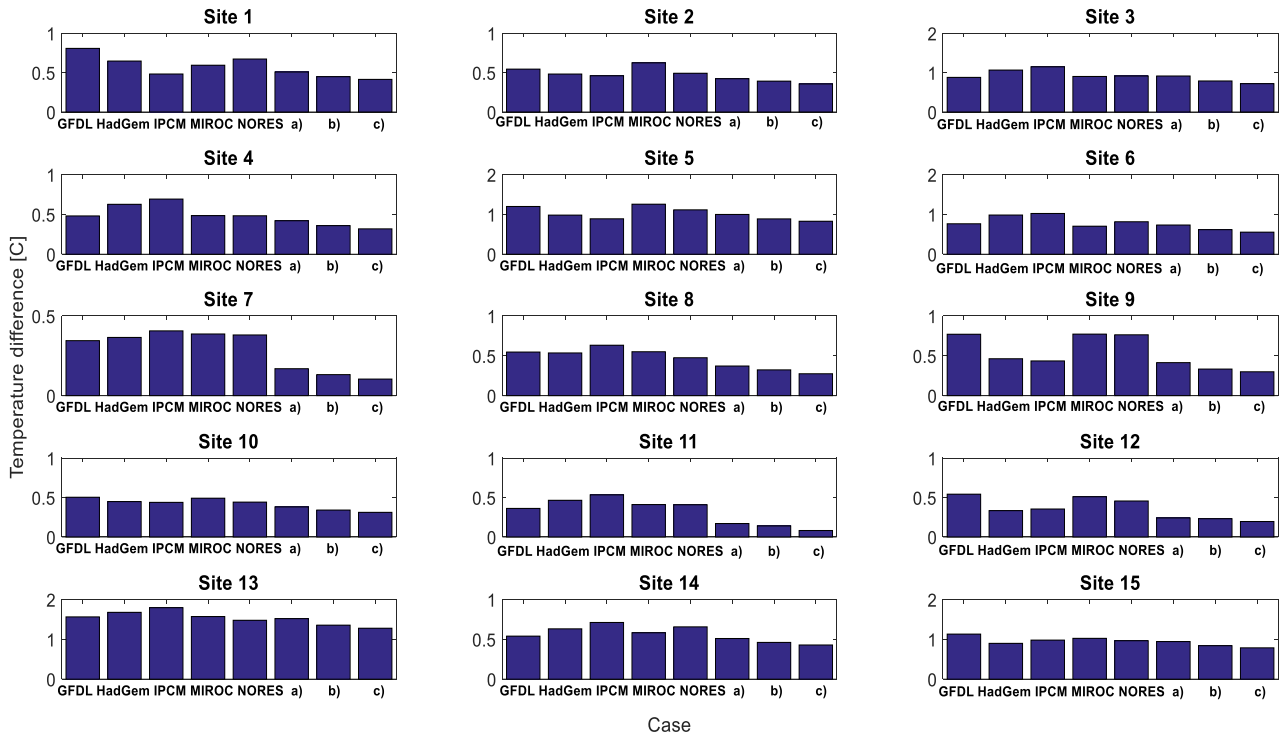


Fig. 7 Annual mean error of the climate change models and their ensembles considering the time interval from 1981 to 2005. Site numbering based on [28].

Finally, it is worth pointing out that the ensemble strategies are expected to improve the accuracy with respect to the individual climate models, but not to address and quantify the epistemic uncertainty of the climate models used themselves. This is because, neither air temperature distributions nor ranges of temperature projections are available, which would allow propagating uncertainty, e.g. with probabilistic and possibilistic approaches [46, 47]. Therefore, in what follows, we limit the analysis to the probabilistic uncertainty propagation of the design input variables of the TH model and of the environmental pressure, A , neglecting the uncertainty on the ensemble temperature projections.

4. Risk assessment of the NPP

The air temperature projections provided by climate models and ensemble strategies for the time intervals t_2 , t_3 and t_4 are used as input data of two risk assessment approaches to assess the risk of the

NPP of Section 2 [28], namely the integrated probabilistic safety assessment and the risk-based classification approach. These approaches have been selected because, although, both approaches rely on the same assumptions and are based on the probabilistic assessment of a dynamic system model, they differ in how uncertainty in output is quantified and, thereby, communicated. On one hand, the integrated probabilistic risk assessment has been shown in [28] to be useful when the knowledge available is strong enough for uncertainty to be quantified as conditional probabilities given a future air temperature [49] (although these probabilities do not capture the uncertainty in climate data). On the other hand, the risk-based classification of projected temperatures communicates uncertainty as statements associated to a future state, as either safe or non-safe, and differences between different climate projections. The difference with the probabilistic risk assessment is that no probabilities are shown, only the projected temperatures, and it may be easier for a decision maker to relate to a temperature than to a probability.

In details, the approaches can be summarized as follows:

1. The integrated probabilistic safety assessment conditional on climate projections: this approach aims at computing the Conditional Functional Failure Probability (CFFP) (i.e., the probability that the pressure of the containment, Y , exceeds the safety threshold of 0.4 MPa) by using a Monte Carlo (MC) procedure. The MC procedure requires sampling, for each month $i = 1, 2, \dots, 12$, and each time interval $t = t_m$, with $m = 1, 2, 3, 4$, $N = 200$ samples of the 24 design input variables and the air pressure A (which is correlated to the air temperature T , that can be provided by either the individual climate models or by their ensembles). Then, each sample is used as input of the TH model of the PCCS to build the parametric distribution of the containment pressure Y , through a Finite Mixture Model (FMM) strategy [48]. The FMM is adopted in order to obtain a robust reconstruction of the probability distribution of Y , with limited number of TH code simulations. This way, both sources of uncertainty (epistemic uncertainty, associated with the PCCS design input variables, and aleatory uncertainty, associated with the natural variability of the environmental condition variable (A)) are quantified by using probability distributions of the input parameters.
2. The risk-based classification on an assessment of critical temperatures: this method aims at classifying the PCCS behaviour with respect to risk-relevant temperature intervals, which are assessed independently from climate projections (i.e., based on actual temperatures and pressures). Once that the risk-relevant temperatures are identified, the projections of the climate models and their ensembles can be embedded into the safety assessment in a straightforward way. The risk-relevant temperature are assessed by analysing the T - Y profile

(i.e., how the profile of the containment pressure Y changes by varying the air temperature T), which is obtained by the simulation of the TH model given all uncertainties (i.e., design input variables D and air pressure A) with fixed T . It is worth noticing that under these premises, the calculated Y depends only on T , because the sampled design variables D are fixed for all the simulations, and A is conditionally dependent on T .

In what follows, we show that the air pressure A is correlated to T . Without loss of generality, let us consider the Sanmen NPP: Fig. 8 shows that T_i^{real} (solid line in Fig. 8) and the corresponding air pressure (dashed line in Fig. 8), which have also been collected in a weather station nearby the NPP, are negatively correlated, that is, an increase of T leads to a decrease of A .

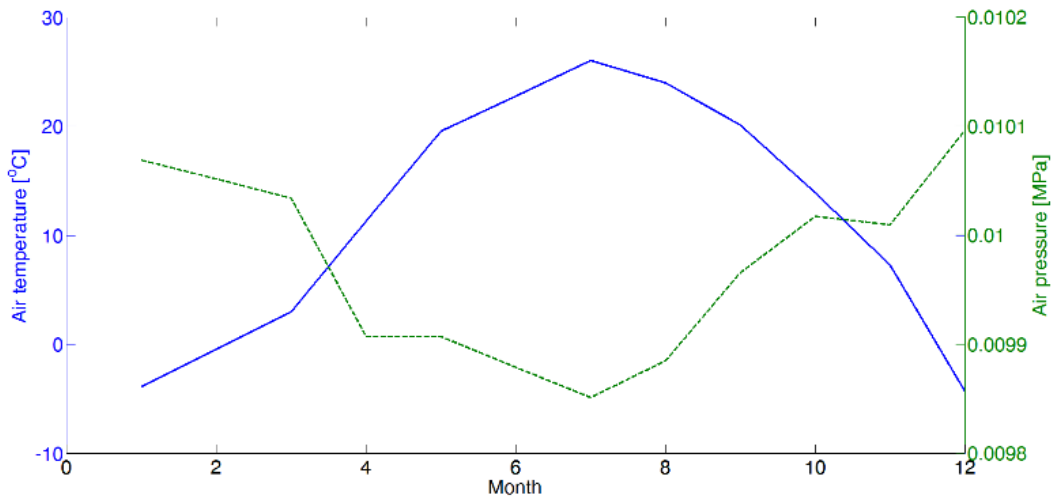


Fig. 8 Monthly mean of air temperatures (solid) and air pressures (dashed) based on observations collected by a Chinese weather station.

For this reason, A is here sampled from the joint distribution of the air temperature and the air pressure. Regarding the Sanmen NPP, the joint distribution of air temperature and pressure is approximated by the monthly specific Gaussian bivariate distribution shown in Fig. 9. Fig. 10 shows that, in this way, samples of A at different future air temperatures $T_i^{projected}$ are also negatively correlated to T .

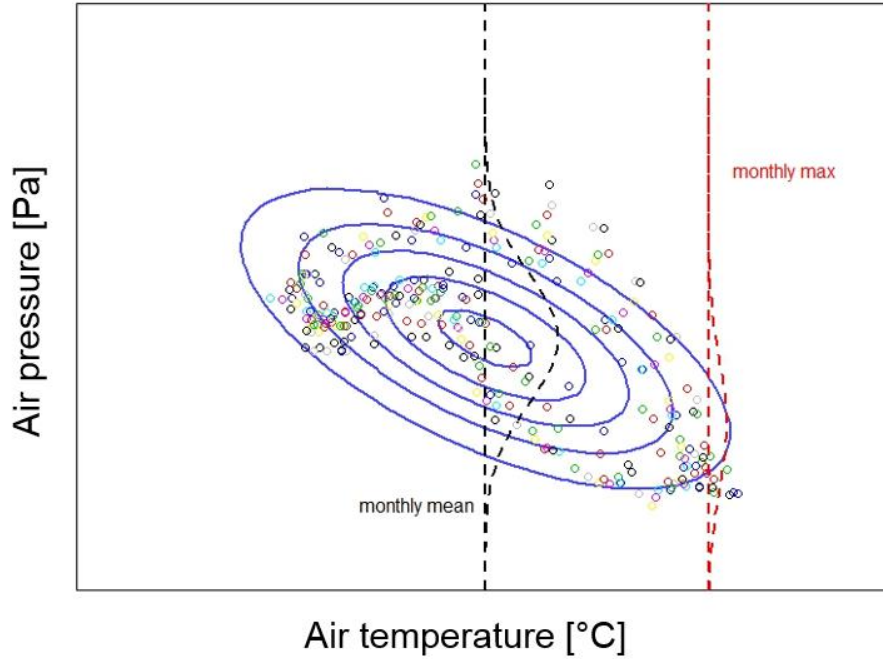


Fig. 9 The joint distribution of temperature and pressure based on data collected by a Chinese weather station (circles).

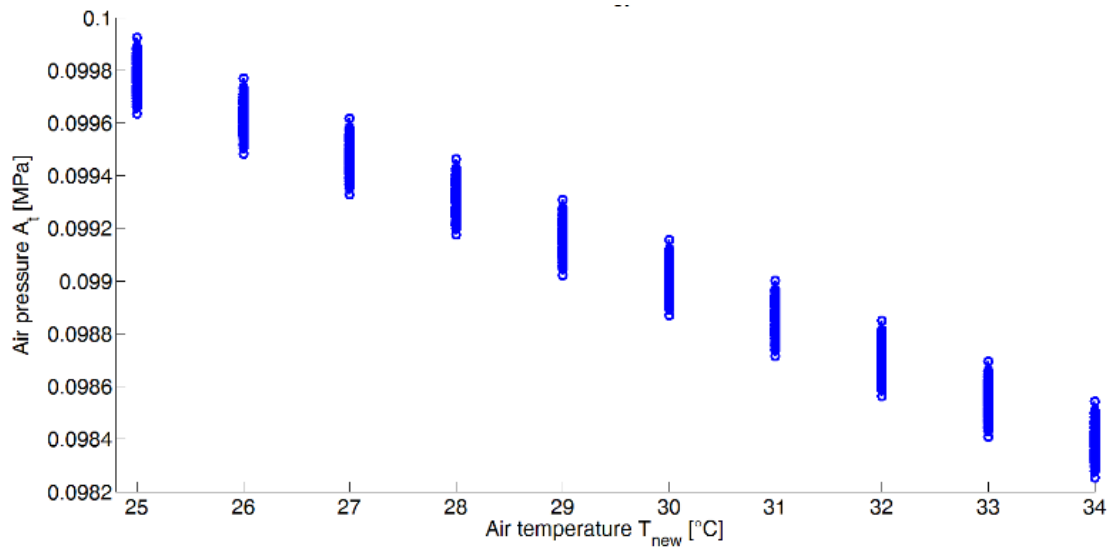


Fig. 10 Samples of air pressure for different air temperatures in the future ($T^{\text{projected}}$) using the Gaussian bivariate distribution.

5. Results

Hereafter, without loss of generality, we show and discuss the results of the application of the two alternative risk assessment approaches to site 1 (the NPP in Samen County, Zhejiang Province, China) and to site 11, (the Duke's Lee NPP, in Gaffney, South Carolina, USA). These NPPs are selected

because of their significance: the former has already been studied in different environmental conditions and climate change scenarios [22; 28], and it is interesting to investigate how risk assessment might be affected by the information carried by the ensembles of climate models, rather than by the individual models [28]; the latter, instead, is interesting to be analysed because, as shown in Fig. 7, it shows the best results in predicting the real historical air temperature by adopting the proposed ensemble strategies.

5.1 Approach 1: The integrated probabilistic safety assessment conditional on climate projections

In order to assess the CFFP of the PCCS, the MC procedure is performed for each individual climate change model and each ensemble strategy by sampling $N = 200$ times, for each month $i = 1, 2, \dots, 12$, and each time interval $t = t_m$, with $m = 1, 2, 3, 4$, the 24 design input variables and the air pressure, A , from the bivariate Gaussian distribution relative to the location of the plant. **It is worth pointing out that the low number of simulations, N , of the TH model is allowed by the successive use of the FMM for robustly reconstructing the probability distribution of Y , even with a limited number of TH code simulations [28, 48].** The environmental parameters (air temperature and pressure) depend on local data, whereas the D design parameters of the NPP are sampled from the distributions presented in Table 2, for each NPP of Fig 2. The results of the MC simulations are, then, used as input of a FMM algorithm, which provides an estimation of the probability distribution of containment pressure Y at each of the four time intervals from 1980 to 2099. Fig. 11 shows the probability distributions (based on the maximum temperature projection $T_{max}^{projected}$) for the three hottest months (July, August and September) in the NPP of site 1. It can be seen that the behaviour of the PCCS is strongly influenced by the air temperature projections used as input of the TH model. For example, in July and August (of the first time interval t_1) the containment pressure Y strongly depends on which climate model or ensemble strategy is used as input of the TH model: the FMM of the containment pressure obtained with the MIROC and NORES climate models (circles and squares lines, respectively, in Fig. 11) is centred on 0.1 MPa, whereas those retrieved by adopting all the ensemble strategies and the GFDL, HadGem and IPCM climate models are shifted towards higher Y values. This also occurs in September (of the fourth time interval t_4) where the GFDL, MIROC and NORES climate models (pointing-down triangles, circles and squares lines, respectively, in Fig. 11) lead the containment pressure probability distribution to be centred to 0.1 MPa, whereas, the other climate models

(HadGem and IPCM) and all the three ensemble strategies lead the containment pressure close to the safety limit of 0.4 MPa.

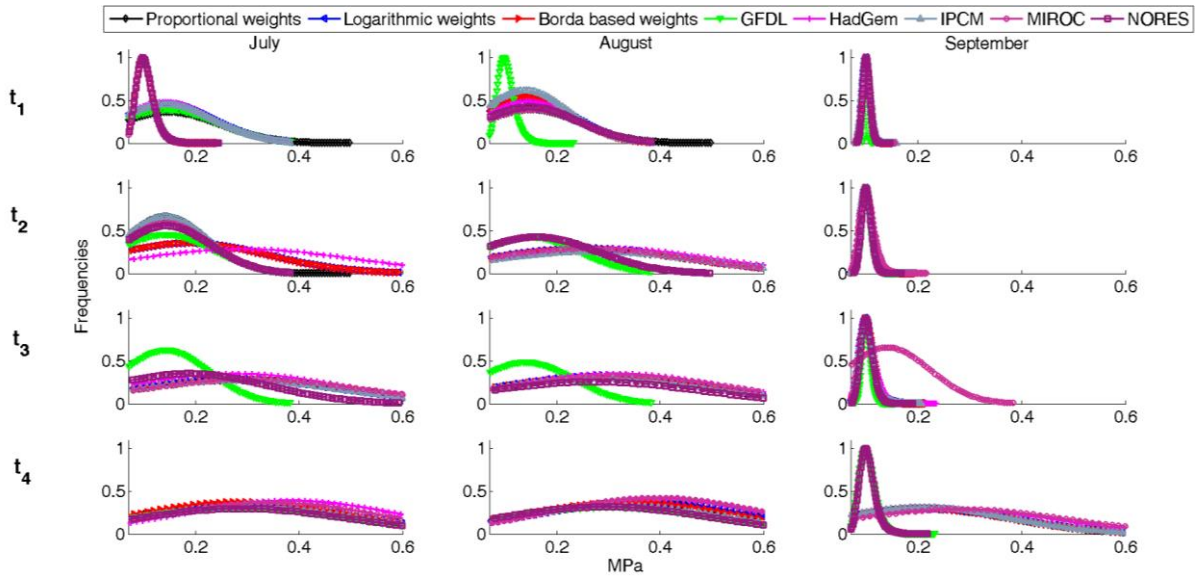


Fig. 11 FMMs of containment pressure (Y) for four time intervals during 1980 to 2099 for site 1, based on the projections of the individual climate models and their ensemble strategies.

Similarly, Fig. 12 shows the FMMs of the containment pressure of 5 months (from May to September during the time periods from 1981 to 2099). Although good agreement of the FMMs retrieved by using climate models and ensemble strategies is shown in the hottest months (June, July and August), with the exception of the HadGem climate model which leads to more likely high containment pressure (crosses line in Fig. 12), the influence of the climate models on the probability distribution of the containment pressure is confirmed by the FMMs of September: in particular, the CFFP of the PCCS largely deviates when the HadGem and NORES climate models are adopted (crosses and squares lines, respectively, in Fig. 12), leading the average containment pressure close to the safety limit of 0.4 MPa. Finally, it is important to point out that differences in the probability distributions of the PCCS are smoothed out when the projections are provided by the three ensembles (diamonds, pointing-forward and pointing-backward triangle lines, for strategy a), b), and c), respectively, in Fig. 12).

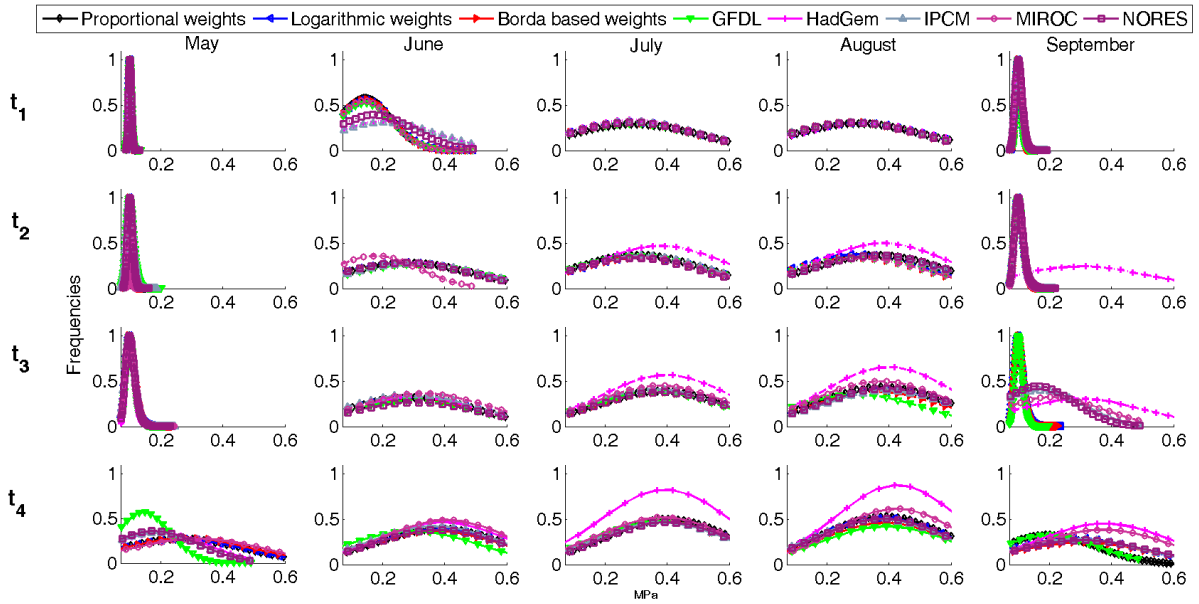


Fig. 12 FMMs of the containment pressure (Y) for four time intervals during 1980 to 2100 for site 11, based on the projections of the individual climate models and their ensemble strategies.

Figures 13 and 14 show, for sites 1 and 11, respectively, the CCFP (i.e., the probability that the FMMs exceed the safety threshold of 0.4 MPa). In general terms, the CFFPs increase as the air temperature projections increase. It is straightforward that also the CFFPs strongly depend on the model chosen to provide the temperature projections: for example, the GFDL model (pointing-up triangles line in Fig. 13) gives low projection of the CFFP, whereas the HadGem model (crosses line in Fig. 13) leads to extremely high projection of the CFFP. On the other hand, the three ensemble strategies (diamonds, pointing-forward and pointing-backward triangle lines, for strategy *a*), *b*), and *c*) in Fig. 13, respectively) show similar projections of the CFFPs, which are neither conservative nor optimistic with respect to those provided resorting to the individual models. Similar results are shown in Fig. 14 for the NPP of site 11.

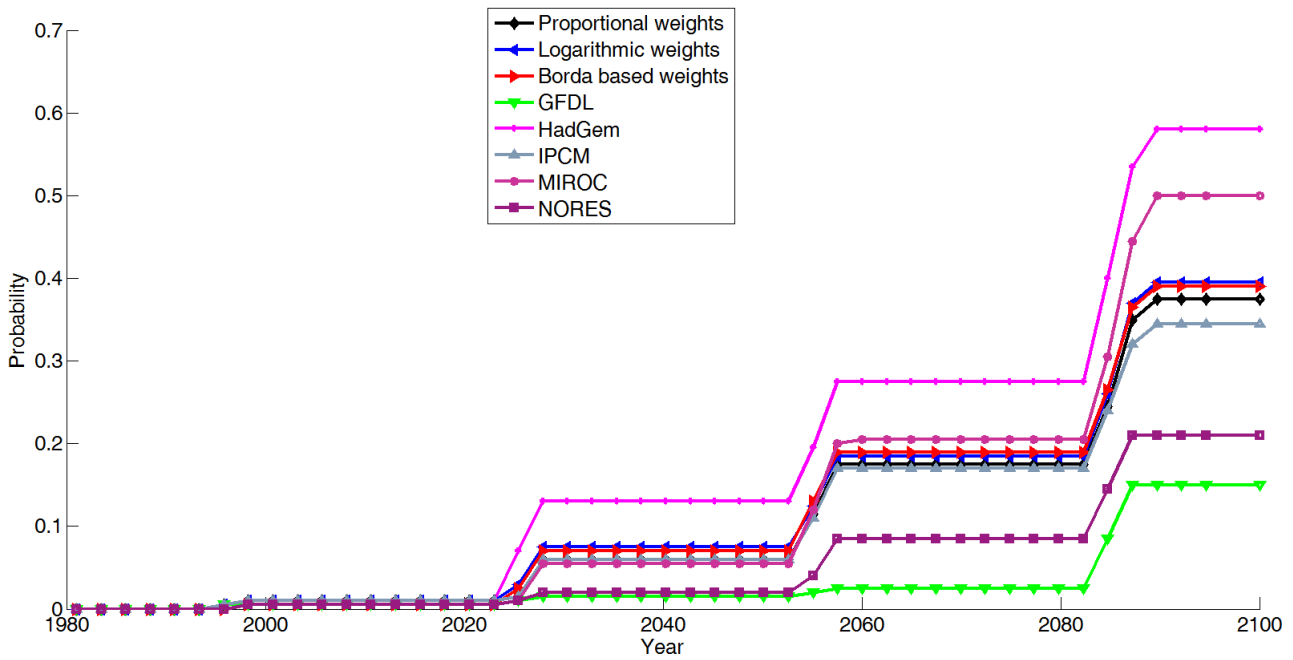


Fig. 13 CFFPs projections using individual climate models and their ensemble strategies, for the NPP of site 1.

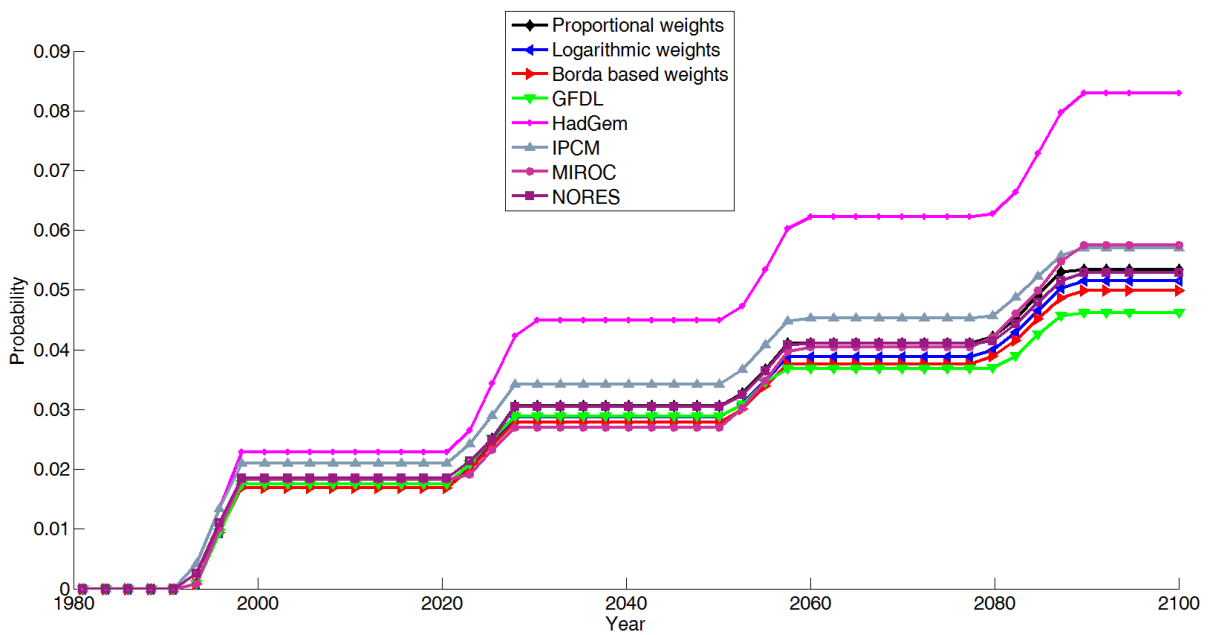


Fig. 14 CFFPs projections using individual climate models and their ensemble strategies, for the NPP of site 11.

In all cases, we claim that the risk assessment performed with the ensemble strategies of the air temperature models can give more reliable (robust) results than that performed with the individual modes, because the ensemble strategies show larger accuracy than the individual climate models in predicting the air temperature, as described in Section 3. **A more insightful uncertainty analysis of**

the CFFPs projections would have been allowed if the uncertainty on the climate projections would have been provided either in terms of probabilistic or possibilistic terms, as already discussed in Section 3.4.

5.2 Approach 2: The risk classification based on an assessment of critical temperatures

The approach consists in assessing the T - Y profiles by simulating the system model given all uncertainties (i.e., design input variables D and air pressure A) with fixed T , where we define the distribution of Y conditional on temperature T (taking into account that air pressure A is conditionally dependent on air temperature T). The distribution of Y is derived by simulating the TH model for temperatures in the range 25°C to 45°C (i.e., the variability of the historical air temperatures on sites 1 and 11), with a fixed set of randomly sampled design variables D . In this way, the differences in Y for different values of T should only depend on T . Figure 15 shows that the relationship between Y and T is monotone: the larger T , the larger the probability of exceeding the safety limit of 0.4 MPa. It can be seen that when T is lower than 30°C the probability of Y to be lower than 0.1 MPa (dashed line in Fig. 15) is approximately 1, whereas when T exceeds 32°C the distribution of Y becomes bimodal with the values 0.10 and 0.55 MPa as the two modes (dashed and continuous lines, respectively, in Fig. 15), where the upper mode is the result of a rule in the TH model that interrupts the calculations when the pressure exceeds 0.55 MPa.

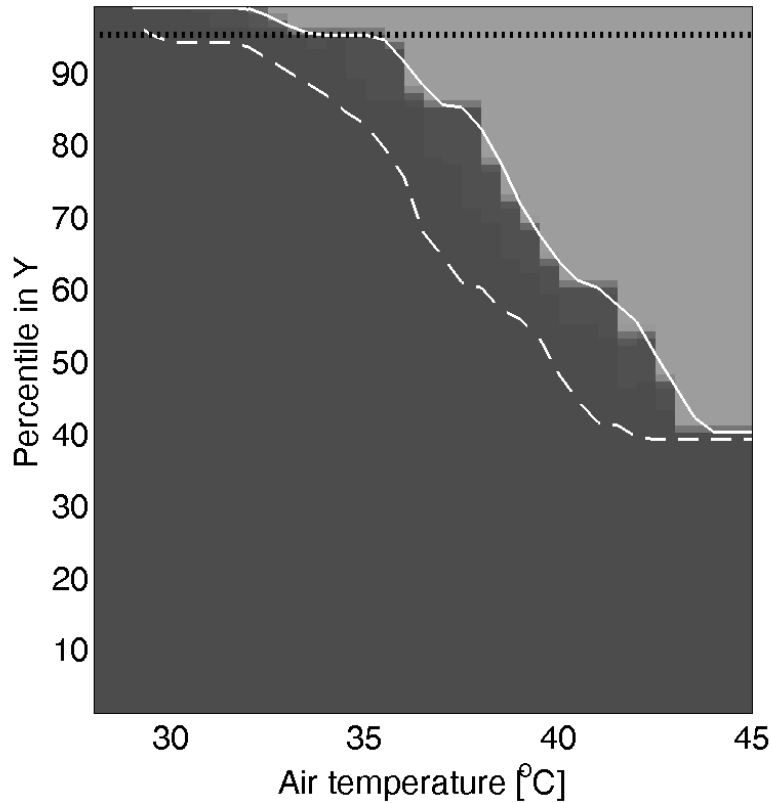


Fig. 15. Profiles of $T - Y$: probability distributions of Y conditional on T with the percentiles for two critical pressures $Y \leq 0.10$ MPa (dashed white) and $Y \geq 0.4$ MPa (solid white).

Fig. 16 and Fig. 17 show the evolution of the 95th percentile of the distribution of Y for site 1 and site 11, respectively. The critical temperatures are found by fixing the safe pressure threshold (Y_l) at 0.1 MPa and the failure pressure threshold (Y_h) at 0.4 MPa, as shown by dotted lines in Figs. 16 and 17. For site 1, as soon as the air temperature T exceeds 28.5 °C, the containment pressure Y increases. On the other hand, the analysis of the distribution of Y for site 11 shows that the containment pressure Y increases as the air temperature T exceeds 30 °C (Table 2). The failure pressure threshold (Y_h) of 0.4 MPa is overcome at different temperatures depending on the site: 35.5°C is identified as the failure critical temperature for site 1 (Fig. 16), whereas the failure critical temperature of site 11 is 36 °C (Fig. 17).

Table 2 Critical temperatures for risk-based classification.

Location	SAFE	CAN FAIL	FAILS
Site 1	$T^{projected} < 28.5^{\circ}\text{C}$	$28.5^{\circ}\text{C} < T^{projected} < 35.5^{\circ}\text{C}$	$T^{projected} > 35.5^{\circ}\text{C}$
Site 11	$T^{projected} < 28.5^{\circ}\text{C}$	$28.5^{\circ}\text{C} < T^{projected} < 35.5^{\circ}\text{C}$	$T^{projected} > 36^{\circ}\text{C}$

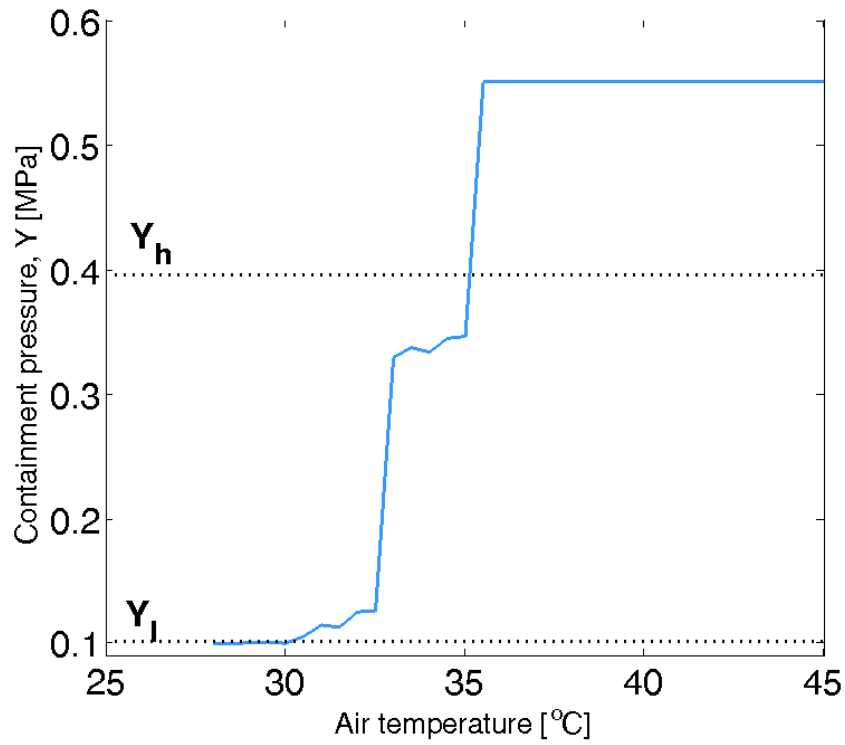


Fig. 16 The critical temperatures leading to the 95th percentile of Y exceeding the safety limit for site I.

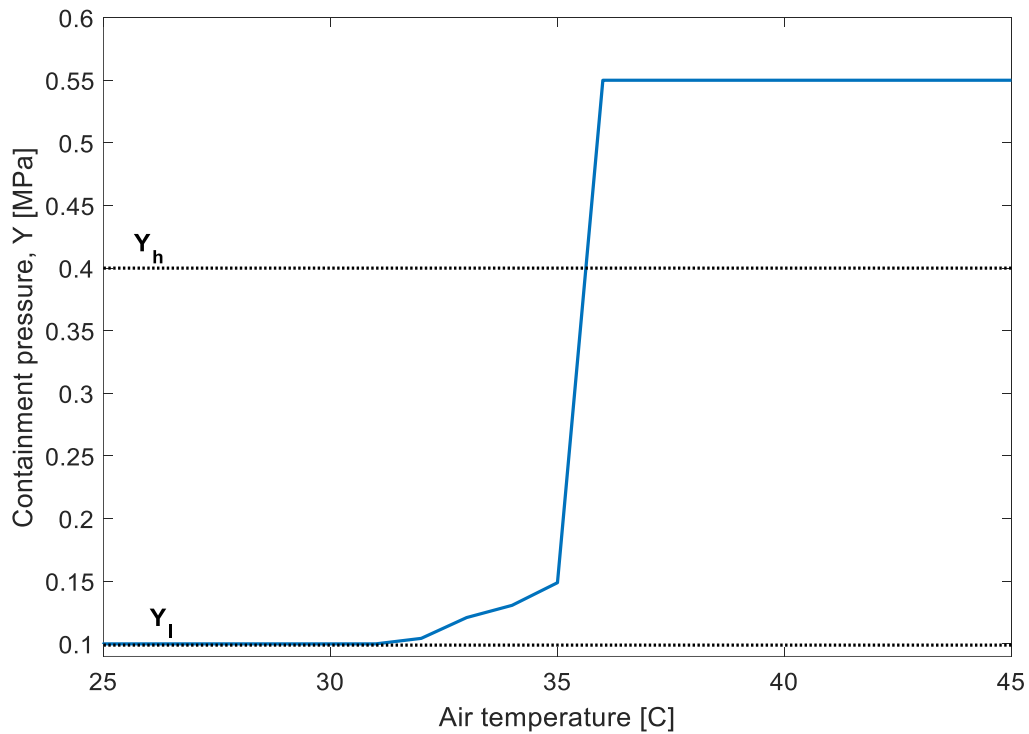


Fig. 17 The critical temperatures leading to the 95th percentile of Y exceeding the safety limit for site II.

The risk classification based on the $T_{max}^{projected}$ projections provided by both the climate models and the ensemble strategies is performed for the hottest months (for the NPPs located at sites 1 and 11). Fig. 18 shows the risk classification for the site 1: even if the forecasts of the air temperature are within the identified risk-relevant interval, the air temperature forecasts provided by the ensemble strategies (diamonds, backward-pointing and forward-pointing triangles in Fig. 18 for the *a*), *b*) and *c*) ensemble strategies, respectively) are very close to one another, whereas, those retrieved by using the individual climate models greatly differ from each other. For example, the projections of the HadGem and MIROC models (crosses and circles in Fig. 18, respectively) are higher than those provided by the NORES climate model (squares in Fig. 18).

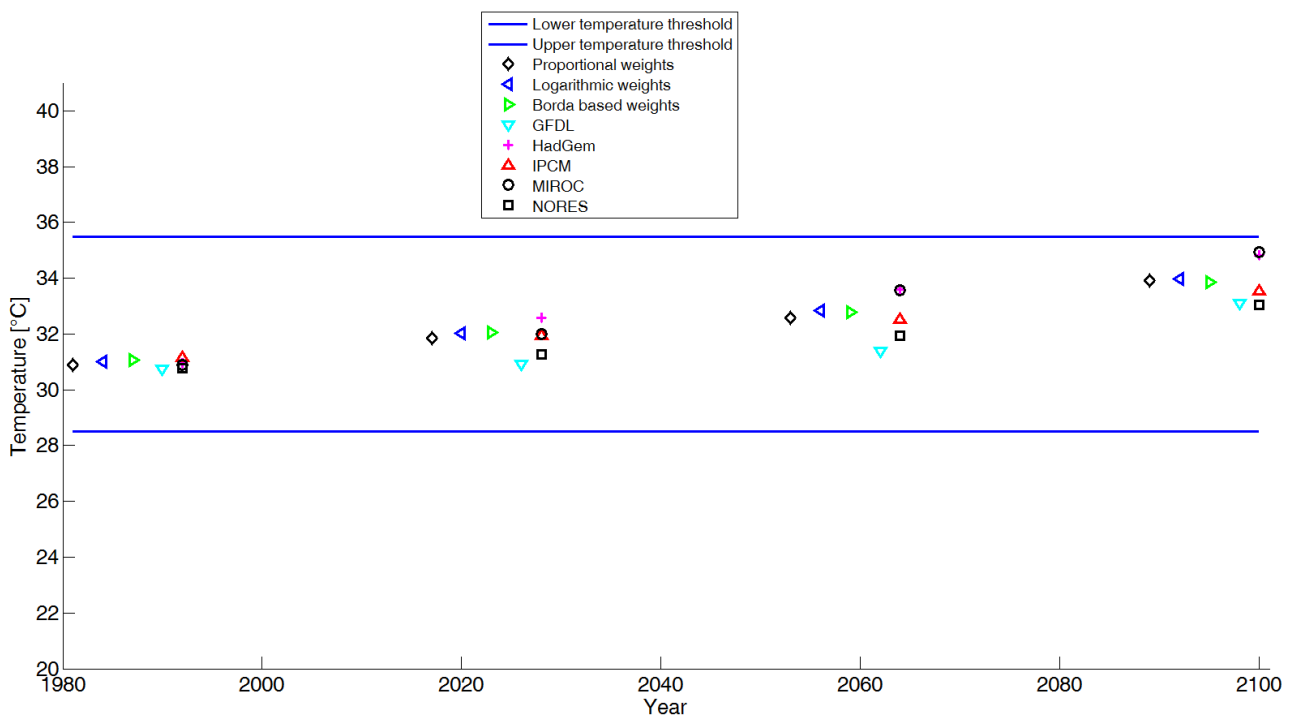


Fig. 18 Risk classification of the $T_{max}^{predicted}$ projections from the five climate models for the hottest month at every location for site 1.

Fig. 19 shows the risk classification of forecast air temperatures of site 11: climate change might have a negative effect on the cooling capacity of the PCCS of site 11, because the projections of the air temperature retrieved by using both climate change models and ensemble strategies are very close to the failure critical temperature of 36 °C. Again, the ensemble strategies (diamonds, back-pointing and forward-pointing triangles in Fig. 19 for the *a*), *b*) and *c*) ensemble strategies, respectively) give very similar air temperature forecasts, whereas the climate models provide different projections of the air

temperature. For example, the HadGem model (crosses in Fig. 19) gives the highest forecasts of the air temperature, which are close to the failure critical temperature from the time period t_2 (from 2011 to 2040). The climate models GFDL, IPCM, MIROC and NORES (pointing-up triangles, pointing-down triangles, circles and squares in Fig. 19, respectively) provide air temperature forecasts that are lower than those provided by the ensembles, and, thus, this may lead to underestimating the risk associated to the PCCS. For example, analyzing the time period t_4 (from 2081 to 2099), it can be observed that the projections provided by these climate models are closer to the safety threshold of 36 °C than those provided by the ensemble strategies.

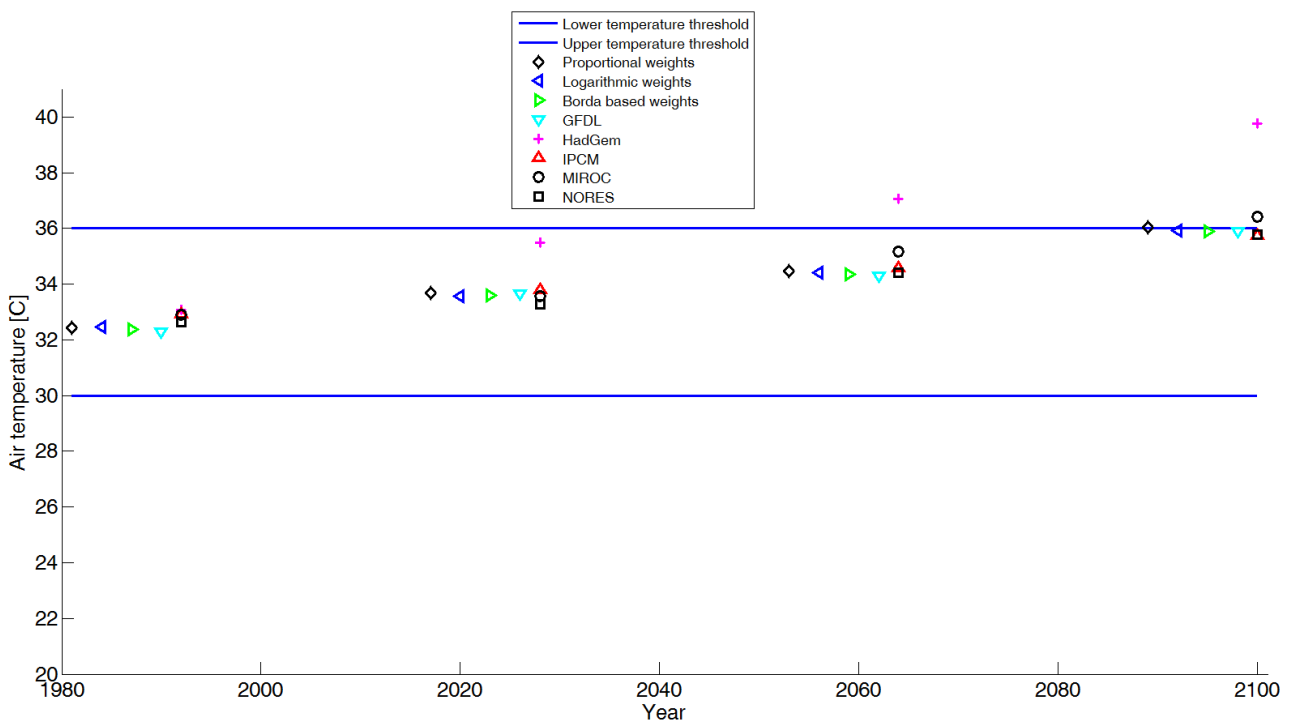


Fig 19 Risk classification of the $T_{max}^{predicted}$ projections from the five climate models for the hottest month at every location for site 11.

Finally, it is worth highlighting the simplicity of application and the limited computational burden of the risk classification approach embedding climate change into the risk assessment: indeed, once that the air temperature projections of the different climate models (with and without the ensemble) are compared with the critical temperatures, the risk associated to that temperature is easily provided (without the need of building the CFFPs, as for approach 1). Limitations of the integrated probabilistic safety assessment conditional on climate projections are indeed overcome: while a probability distribution of the climate data is strongly required by the probabilistic safety assessment approach, this is not required by the risk-based classification approach. Since future climate data are pointwise projections, i.e., without probability distribution, the risk assessment approach might turn to be

challenged as the number of system variables depending on the air temperature increases, whereas the risk-based classification approach would not.

6. Conclusions

Climate change must be considered for NPPs, in particular if passive safety systems are used. To support this claim, we have considered as case study a PCCS of an AP100 reactor. Several challenges with the integration of climate change have been identified and two alternative ways to investigate the potential impact of changing climate have been proposed: a fully probabilistic modelling based on climate projections and a risk classification-based on an assessment of critical temperatures. The probabilistic risk assessment quantifies the failure probability of the NPP, conditioned to a future air temperature. Conversely, the risk classification of projected temperatures provides a risk assessment of the NPP under future climate scenarios, by providing the future air temperatures which may lead the PCCS into failure. From a decision maker point of view, we expect this latter method to be preferred, because temperature is a physical variable more easy to understand than the concept and meaning of probability.

Three ensemble approaches, based on the aggregation of the projections of five climate models, have been proposed to be used within two alternatives ways of investigation. It has been demonstrated that, using a database of real recorded air temperatures, the three ensemble approaches give more accurate forecasts than the individual climate models. Results have shown that, whilst each individual climate model leads to a different risk assessment, the ensemble strategies lead to very similar risk assessment results and, consequently, the evaluation of the risk is more robust than that one obtained by using an individual climate model, due to the fact that the results do not depend on the particular climate change model.

7. Acknowledgment

Authors thank Dr. Sahlin Ullrika for her precious encouragement in initiating the research activity, for initially manipulating the climate change data, and for the fruitful exchanges of views that have greatly improved the manuscript.

References

- [1] Anderson, B., Borgonovo, E., Galeotti, M., et al. Uncertainty in climate change modeling: Can global sensitivity analysis be of help?, *Risk Analysis*, 2014; 34 (2), 271-293.
- [2] Rummukainen, M., Climate change: changing means and changing extremes, *Climate Change*, 2013;121: 3-13.
- [3] Webster, M.D., Sokolov, A.P., A methodology for quantifying uncertainty in climate projections, *Climatic Change*, 2000; 46 (4), pp. 417-446.
- [4] Singh, R.P., Causes and consequences of the greenhouse gases, *Bulletin of Pure and Applied Sciences - Section F Geological Sciences*, 2006; 25 (1-2), pp. 13-17.
- [5] Carlsson-Kanyama, A., González, A.D., Potential contributions of food consumption patterns to climate change, *American Journal of Clinical Nutrition*, 2009; 89 (5), pp. 1704S-1709S.
- [6] Spiegelhalter, DJ., Riesch, H., Don't know, can't know: embracing deeper uncertainties when analysing risks, *Philosophical Transactions of the Royal Society A: Mathematical, Physical and Engineering Sciences*, 2011; 369: 4730-50.
- [7] Zio, E., Di Maio, F., et al., Safety margins confidence estimation for a passive residual heat removal system, *Reliability Engineering and System Safety*, 2010; vol. 95, 828–836.
- [8] Asian Development Bank, Climate risk and adaptation in the electric power sector, Mandaluyong City, Philippines: Asian Development Bank, 2012.
- [9] Droguett, E.L., Mosleh, A., Integrated treatment of model and parameter uncertainties through a Bayesian approach, *Proceedings of the Institution of Mechanical Engineers, Part O: Journal of Risk and Reliability*, 2013, 227 (1), pp. 41-54.
- [10] López Droguett, E., Mosleh, A., Bayesian treatment of model uncertainty for partially applicable models, *Risk Analysis*, 2014, 34 (2), pp. 252-270.
- [11] Baraldi P, Zio E., A comparison between probabilistic and Dempster-Shafer theory approaches to model uncertainty analysis in the performance assessment of radioactive waste repositories. *Risk Analysis*, 2010; 30:1139–1156.
- [12] Pourgol-Mohamad M, Mosleh A, Modarres M., A methodology for the use of experimental data to enhance model output uncertainty assessment in thermal hydraulics codes, *Reliability Engineering and System Safety*, 2010; 95:77–86.
- [13] Hoefer A, Dirksen G, Eyink J, Pauli EM., Uncertainty treatment for level-2 probabilistic safety analysis, *Nuclear Science and Engineering*, 2010; 166(3):202–217.
- [14] Martin, G.M., Bellouin, N., Collins, W.J. et al., The HadGEM2 family of Met Office Unified Model climate configurations”, *Geoscientific Model Development*, 2011; 4 (3), 723-757.
- [15] R. Polikar, Ensemble based systems in decision making, *Circuits Syst. Mag. IEEE*, 2006; vol. 6 (3), 21–45.
- [16] F. Di Maio, J. Hu, P. Tse, et al. Ensemble-approaches for clustering health status of oil sand pumps, *Expert Systems with Applications*, 2012; 39 (5), 4847–4859,
- [17] Tebaldi, C., Knutti, R. The use of the multi-model ensemble in probabilistic climate projections, *Phil. Transactions of the Royal Society A: Mathematical, Physical and Engineering Sciences*, (2007); 365 (1857), 2053-2075.
- [18] S. Al-Dahidi, F. Di Maio, et al., A novel ensemble approach for clustering operational transients of a NPP turbine, *International Journal of Prognostics and Health Management*, 2015; 6 (Special Issue Nuclear Energy PHM), ISSN 2153-2648.
- [19] M. Hoseyni, F. Di Maio, M. Vagnoli, et al., A Bayesian ensemble of sensitivity measures for Severe Accident modeling, *Nuclear Engineering and Design*, 2015; 295, 182–191.
- [20] F. Di Maio, A. Bandini, E. Zio, et al., Bootstrapped Ensemble-based Sensitivity analysis of a TRACE thermal-hydraulic model based on a limited number of PWR large Break LOCA simulations, *Reliability Engineering and System Safety* Volume, 2016; 153, 122–134.
- [21] S. Al-Dahidi, F. Di Maio, P. Baraldi, et al., A Locally Adaptive Ensemble Approach for Data-Driven Prognostics of Heterogeneous Fleets, *Journal of Risk and Reliability*, Special issue of ESREL 2015.

- [22] Di Maio, F., Nicola, G., Zio, E., et al., Ensemble-based sensitivity analysis of a Best Estimate Thermal Hydraulics model: Application to a Passive Containment Cooling System of an AP1000, Nuclear Power Plant. *Annals of Nuclear Energy*, 2014; 73, 200–210.
- [23] IAEA, Climate change and nuclear power 2015, International Atomic Energy, Vienna, 2015.
- [24] Wan, P.K., Carson, A.C., Chan, D.W., “Climate change considerations in sustainable development of nuclear power plants in the united states”, International Conference on Nuclear Engineering, Proceedings, ICONE, May 17–21, 2010, Xi’an, China, vol. 6, pp. 403-407.
- [25] Rubbelke, D. and Vogele, S., Impacts of climate change on European critical infrastructures: The case of the power sector, *Environmental Science & Policy*, 2011; 14: 53-63.
- [26] Linnerud, K., Mideksa, TK. and Eskeland, GS., The Impact of Climate Change on Nuclear Power Supply, *Energ J.*, 2011; 32: 149-68.
- [27] Kopytko, N. and Perkins, J., Climate change, nuclear power, and the adaptation-mitigation dilemma, *Energy Policy*, 2011; 39: 318-33.
- [28] Sahlin, U., Di Maio, F., Vagnoli, M., et al., Evaluating the impact of climate change on the risk assessment of Nuclear Power Plants, Safety and Reliability of Complex Engineered Systems - Proceedings of the 25th European Safety and Reliability Conference, ESREL 2015, 7-10 Sept. 2015, pp. 2613-2621.
- [29] Yu Yu, Shengfei W., Fenglei N., Thermal-hydraulic performance analysis for AP1000 passive containment cooling system, Proceedings of the 21th International Conference on Nuclear Engineering ICONE21 July 29-August 2, Chengdu, Sichuan, China, 2013.
- [30] Schulz, T.L., Westinghouse AP1000 advanced passive plant, *Nuclear Engineering and Design*, 2006; 236. 1547–1557.
- [31] IAEA. Defining initiating events for purposes of probabilistic safety assessment. IAEA, IAEA-TECDOC-719, Vienna, ISSN 1011-4289, 1993.
- [32] Rahim, F.C., Rahgoshay, M., Mousavian, S.K., “A study of large break LOCA in the AP1000 reactor containment”, *Progress in Nuclear Energy*, 2012; 54 (1), 132–137.
- [33] Yu, Y., Ma, G., Hao, Z., et al., Correlation analysis for screening key parameters for passive system reliability analysis, *Annals of Nuclear Energy*, 2015; 77.
- [34] Burgazzi, L., Evaluation of uncertainties related to passive systems performance, *Nuclear Engineering and Design*, 2004; 230, 93–106.
- [35] Taylor K. E., Stouffer R. J., Meehl G. A., 2012: An overview of CMIP5 and the experiment design. *Bulletin of the American Meteorological Society*, 93, 485-498
- [36] Ng, B., Cai, W., Walsh, K. Nonlinear feedbacks associated with the Indian Ocean dipole and their response to glob-al warming in the GFDL-ESM2M coupled climate model”, *Journal of Climate*, 2014; 27 (11), 3904-3919.
- [37] Dufresne, J.-L., Foujols, M.-A., Denvil, S., et al., Climate change projections using the IPSL-CM5 Earth System Model: From CMIP3 to CMIP5, *Climate Dynamics*, 2013; 40 (9-10), 2123-2165.
- [38] Watanabe, S., Yokohata, T. Future increase in the all-sky UV-B radiation over asia projected by an earth system model, *Journal of the Meteorological Society of Japan*, 2012; 90 (A), 295-305.
- [39] Sandø, A.B., Gao, Y., Langehaug, H.R., Poleward ocean heat transports, sea ice processes, and Arctic sea ice variability in NorESM1-M simulations”, *Journal of Geophysical Research: Oceans*, 2014; 119 (3), 2095-2108.
- [40] Van Vuuren, D.P., Edmonds, J., Kainuma, M., et al., The representative concentration pathways: An overview, *Climatic Change*, 2011; 109 (1), 5-31.
- [41] Raftery, A.E., Gneiting, T., Balabdaoui, F., Polakowski, M., Using Bayesian model averaging to calibrate forecast ensembles, *Monthly Weather Review*, 2005, 133 (5), pp. 1155-1174.
- [42] P. Baraldi, A. Cammi, F. Mangili, et al., Local Fusion of an Ensemble of Models for the Reconstruction of Faulty Signals, *Nucl. Sci. IEEE Trans.*, 2010; 57 (2), 793–806.
- [43] GISTEMP Team, “GISS Surface Temperature Analysis (GISTEMP)”, NASA Goddard Institute for Space Studies, Dataset at <http://data.giss.nasa.gov/gistemp/>, 2016, (accessed 2016-06-13).
- [44] Hansen, J., R. Ruedy, M. Sato, et al., Global surface temperature change, *Rev. Geophys.*, 2010; 48, RG4004, doi:10.1029/2010RG000345.
- [45] Hansen, J., D. Johnson, A. Lacis, et al., Climate impact of increasing atmospheric carbon dioxide, *Science*, 1981; 213, 957-966.
- [46] Pourgol-Mohammad, M., Thermal-hydraulics system codes uncertainty assessment: A review of the methodologies, *Annals of Nuclear Energy*, 2009, 36 (11-12), pp. 1774-1786.

[47] Baraldi, P., Zio, E., A Combined Monte Carlo and possibilistic approach to uncertainty propagation in event tree analysis, *Risk Analysis*, 2008, 28 (5), pp. 1309-1325.

[48] McLachlan, G., Peel, D., *Finite Mixture Models*, New York: John Wiley & Sons Inc., 2000.

[49] Aven, T., Baraldi, P., Flage, R., et al., *Uncertainty in Risk Assessment: The Representation and Treatment of Uncertainties by Probabilistic and Non-Probabilistic Methods*, *Uncertainty in Risk Assessment: The Representation and Treatment of Uncertainties by Probabilistic and Non-Probabilistic Methods*, Wiley, 2014; 1-186.